

# OPTIMAL LIGHT CURVE ATTITUDE INVERSION WITH MEASUREMENT NOISE: TWO CASE STUDIES

Liam Robinson and Carolin Frueh

Purdue University, West Lafayette, United States, Email: {robin502, cfrueh}@purdue.edu

## ABSTRACT

Understanding the orientation and angular velocity state of active or passive human-made space objects is critical for many space situational awareness operations like long-term orbit propagation, anomaly resolution, determining mission status, and active debris removal. Beyond low-Earth orbit, optical telescopes are predominantly used to track space objects. Due to atmospheric distortion and aperture size, it is generally impossible to resolve even large satellites and rocket bodies in optical ground-based imagery. As a result, shape and orientation information is unavailable in individual images, but a measurement of the object's total brightness can still be obtained. Even if the object's shape and reflective properties are known, any given brightness measurement will generally correspond to infinitely many possible orientations. To constrain the solution space, the brightness can be tracked over time – producing a sequence of measurements called a light curve. If the object's identity is known, its attitude profile can be estimated from the light curve – up to certain ambiguities – through a process known as light curve attitude inversion. Due to symmetries in the observation geometry and object shape, there may be multiple attitude profiles that are equally likely to produce any given light curve. Environmental and instrumental measurement noise worsens these ambiguities. To reliably identify these ambiguous solutions, global attitude inversion methods must thoroughly search the solution space.

In this work, we apply a BFGS-based multi-start global attitude inversion algorithm to efficiently solve the attitude inversion problem globally. Results for synthetic observations are presented for a generic upper stage. Results for real observations taken by the Purdue Optical Ground Station of Delta I upper stage and the ECHOSTAR II satellite are also presented. Given a light curve with an estimate of the shape and reflective properties of the object, our procedure searches the space of initial orientations, angular velocities, and inertia tensors to find initial conditions that produce light curves with low error compared to the observed values. Our formulation inherently accounts for the aforementioned ambiguities,

the physical constraints of torque-free rigid body motion, and the noise in the light curve.

**Keywords:** Light curve inversion; Attitude estimation; Photometry; Inverse problems.

## 1. INTRODUCTION

Knowledge of spacecraft orientation and angular velocity states is critical for many space situational awareness (SSA) tasks. Understanding the evolution of high area-to-mass ratio objects [19] and decommissioned satellites [42], planning and executing active debris removal [3], and recovering from mission anomalies [56] all require attitude information.

Methods for estimating the attitude state of uncontrolled space objects from light curves differ significantly depending on the presence of an initial guess. If prior knowledge is available, many filter-based approaches have been developed to process new photometry to update the guess orientation and angular velocity. This class of methods includes single Kalman filters [5, 21, 62], and multi-filter multiple-model adaptive estimation (MMAE) schemes [33, 11]. These approaches can be very effective if the initial state estimate is close to the truth, but have been reported to diverge even in cases when the initial guess is within  $5^\circ$  of the ground truth orientation and  $0.03^\circ \cdot s^{-1}$  in angular velocity error [21] due to measurement nonlinearity and ambiguities.

If no initial attitude guess is available, as in most cases of passive debris observation, the inversion problem must be solved globally. Filtering approaches can be applied here too; particle [32, 25] and Bayesian Multi-Hypothesis filters [5, 57] have shown promise in prior work, but still rely on high-quality priors as with the single-hypothesis Kalman filters. In the absence of any prior knowledge about the object's attitude state, simulated annealing [21, 8], genetic algorithms [21, 39, 8], and particle swarm optimizers (PSOs) [8, 9, 6, 7, 21, 20] can be applied to search the solution space exhaustively.

While much work has performed full state attitude

inversion on simulated light curve data [6, 21, 46], the applicability of many of these methods to real observations is untested. Studies that do work with real data often focus on estimating an assumed constant spin rate and axis of rotation for the observed object. These assumptions are made to simplify the estimation process but can lead to misleading conclusions when the observed object has a complex rotation state.

Frequency analysis in the form of periodograms, Fourier transforms, or epoch folding, is often used to determine the spin rate based on the light curve’s frequency spectrum [52, 53, 26, 49, 41, 64, 28]. If optical material properties are known, the width of a single specular glint can provide sufficient information to determine the rotation rate [24]. There has also been interest in tracking the evolution of spin rates over time for different classes of objects in different orbital regimes [28, 1, 27]. These spin rate determination methods are designed for single-axis rotations and can fail for tumbling objects.

The rotation axis is often estimated for diffusely reflecting objects that are well-approximated as ellipsoids via the so-called amplitude method [63] which has been extended for combined spin and precession motion [64]. For light curves with strong specular peaks, the timing of these glints can be used to determine the constant rotation axis given multiple passes of observations [58, 28]. These approaches are not applicable for generalized rigid body motion where no simplifying assumptions about the location of the spin axis are available.

The simplifying assumptions of constant, single-axis rotation that are commonly made when working with real data enable elegant solutions but break down when the observed object is in a complex spin profile. Methods for full attitude state solutions – time-varying orientation and angular velocities – have been developed [9, 6, 21, 32], but are seldom applied to real data. Works that have been successful at estimating a full rigid-body attitude state from real data include genetic algorithms [40, 22] and brute-force grid search [48]. Any full-state estimation method must tackle the inherent computational complexity, lack of knowledge of material reflectivities, and the presence of measurement noise.

In this paper, we describe a global full-state attitude solver inspired by recent PSO work [6] but is easier to tune, can be fully parallelized, and is robust to significant measurement noise [46]. Further, our method differs from other global estimation methods in that we do not seek to find one optimal solution and instead search for a collection of high-quality local minima to directly study the many ambiguous solutions for a given light curve. Our approach is designed specifically for use with real data as we explicitly take time-varying measurement noise and uncertainties in the body moments of inertia into account.

To solve the optimization problem, we sample many candidate solutions scattered throughout the solution space and perform gradient-based optimization on each using the BFGS algorithm. Our optimization procedure reliably converges to high-quality maximum likelihood estimates of the attitude state. The final output of our method is an array of the best solutions, ranked by their likelihood. Clusters of low-error minima can be analyzed to identify families of solutions.

This work proceeds by describing the inversion method, discussing efficient methods for computing the time-varying probability density of the light curve, and reporting inversion test case results. We present inversion results for a simulated rocket body light curve where the ground truth is available to demonstrate the efficacy of the method, followed by results for real light curve data collected by the Purdue Optical Ground Station for a derelict ECHOSTAR satellite and Delta I rocket body. A deeper treatment of our method and additional simulated light curve results can be found in [46].

## 2. INVERSION METHOD

### 2.1. State Definition and Dynamics

The state vector  $\mathbf{x}$  is defined to be the concatenation of the Modified Rodriguez Parameter (MRP)  $\mathbf{p} = [p_1, p_2, p_3]^T$ , the principal body frame angular velocity  $\boldsymbol{\omega} = [\omega_1, \omega_2, \omega_3]$  in radians per second, and the ratios of the principal moments of inertia  $J_y/J_x$  and  $J_z/J_x$  where the constant inertia tensor in principal axes is  $J = \text{diag}([J_x, J_y, J_z])$ :

$$\mathbf{x} = [p_1 \quad p_2 \quad p_3 \quad \omega_1 \quad \omega_2 \quad \omega_3 \quad J_y/J_x \quad J_z/J_x]^T. \quad (1)$$

The first six elements of the state vector are time-varying with dynamics given by:

$$\dot{\mathbf{p}} = \frac{1}{4} [(1 - \mathbf{p} \cdot \mathbf{p}) + 2\mathbf{p} \times \boldsymbol{\omega} + 2(\boldsymbol{\omega} \cdot \mathbf{p})\mathbf{p}], \quad (2)$$

$$\dot{\boldsymbol{\omega}} = J^{-1} [(J\boldsymbol{\omega}) \times \boldsymbol{\omega} + \mathbf{M}]. \quad (3)$$

We use the Runge-Kutta 4 numerical integration algorithm for all state propagation as it is computationally inexpensive and has low error – usually below  $1^\circ$  over the course of a well-sampled light curve.

### 2.2. Objective Function

Our inversion method is based on the global minimization of a maximum-likelihood loss function

which computes the negative log-likelihood of the observed light curve  $\mathcal{S}$  being a sample from the normal distribution defined by the estimated light curve mean  $\hat{\mathcal{S}}$  and the standard deviation at each  $k$ th timestep  $\sigma_k$ :

$$f(\mathbf{x}) = \frac{1}{m} \sum_{k=1}^m \left[ \frac{1}{2} \ln 2\pi + \ln \sigma_k + \frac{1}{2} \left( \frac{\mathcal{S}_k - \hat{\mathcal{S}}_k(\mathbf{x})}{\sigma_k} \right)^2 \right]. \quad (4)$$

Note that the constant  $0.5 \ln 2\pi$  could be removed from the objective function, but it is retained such that  $\exp(-f(\mathbf{x}))$  is a true likelihood. If the reflectivity of the object's faces is not well-known, we rescale the estimated light curve mean  $\hat{\mathcal{S}}(\mathbf{x})$  to have equal  $\ell_2$  norm to the observations to resolve the inherent albedo-area ambiguity:

$$\hat{\mathcal{S}}(\mathbf{x}) = \frac{\|\mathcal{S}\|}{\|\tilde{\mathcal{S}}(\mathbf{x})\|} \tilde{\mathcal{S}}(\mathbf{x}), \quad (5)$$

where  $\tilde{\mathcal{S}}(\mathbf{x})$  is the original, poorly scaled, estimated light curve. In this work, the light curve and its standard deviation are always assumed to be expressed in a linear unit, e.g., analog-to-digital units (ADU) or irradiance proportional to  $W/m^2$ .

### 2.3. Computing Local Minima

Our multi-start solution method begins by creating  $n_{\text{sample}}$  sampled states scattered throughout the solution space – possibly sampled from a prior distribution based on available knowledge. In the most basic case, the initial states are drawn for sample  $i$  at iteration  $k = 0$ :

$$\mathbf{x}_{0,i}(0) = \begin{bmatrix} \mathbf{p}_{i,0}(0) \\ \boldsymbol{\omega}_{i,0}(0) \\ (J_y/J_x)_{i,0} \\ (J_z/J_x)_{i,0} \end{bmatrix}. \quad (6)$$

In this work, initial state vectors are sampled from a prior distribution, usually defined independently for the MRP, angular velocity, and inertia tensor ratios. If no information is available, as is usually the case, a uniform distribution is sampled from the first six components of the state. In particular,  $\mathbf{p}_{i,0}(0)$  is uniformly randomly sampled from orientation space,  $\boldsymbol{\omega}_{i,0}(0)$  is randomly sampled from a uniform distribution of magnitudes up to  $\|\boldsymbol{\omega}\|_{\text{mid}}$  – the mean angular

rate at which to initialize state samples. We determine this value based on the maximum power positive frequency in the observed light curve  $f^*$  in Hertz as simply  $\|\boldsymbol{\omega}\|_{\text{mid}} = 2\pi f^*$ . Uniformly sampling over angular velocity directions, we can express the default sampling strategy for an angular velocity state as:

$$\boldsymbol{\omega}_{i,0}(0) = \frac{m}{\sqrt{g_1^2 + g_2^2 + g_3^2}} \cdot [g_1 \ g_2 \ g_3]^T, \quad (7)$$

where  $g_{1:3} \in \mathcal{N}(0, 1)$  and  $m = \mathcal{U}(c_1 \|\boldsymbol{\omega}\|_{\text{mid}}, c_2 \|\boldsymbol{\omega}\|_{\text{mid}})$ . The constants  $c_1 < 1$  and  $c_2 > 1$  are chosen to correct for the fact that even for a well-chosen  $\|\boldsymbol{\omega}\|_{\text{mid}}$ , there can still be numerous high-quality solutions at significantly lower or higher angular velocities that possess equal  $f^*$  values. This is a result of object shape symmetries or harmonics in spin and precession rates. We select  $c_1 = 0.5$ ,  $c_2 = 2$  for this work.

For the MRP, we first sample a quaternion  $\mathbf{q}_i(0) = [q_x, q_y, q_z, q_w]^T$  uniformly over orientation space:

$$\mathbf{q}_i(0) = \frac{1}{\sqrt{g_1^2 + g_2^2 + g_3^2 + g_4^2}} [g_1 \ g_2 \ g_3 \ g_4]^T, \quad (8)$$

where  $g_{1:4} \in \mathcal{N}(0, 1)$ , and project the quaternion into MRP space:

$$\mathbf{p}_{i,0}(0) = \frac{1}{1 + q_w} [q_x \ q_y \ q_z]^T. \quad (9)$$

Unlike the MRP and angular velocity, the default sampling method for inertia ratios initial samples  $(J_y/J_x)_{i,0}$  and  $(J_z/J_x)_{i,0}$  draws from independent, identically distributed Gaussian prior distributions with  $\sigma_J$  centered at estimated values derived from the known geometry of the object  $(J_y/J_x)_{\text{est}}$  and  $(J_z/J_x)_{\text{est}}$ , such that:

$$\begin{bmatrix} (J_y/J_x)_{i,0} \\ (J_z/J_x)_{i,0} \end{bmatrix} \sim \mathcal{N} \left( \begin{bmatrix} (J_y/J_x)_{\text{est}} \\ (J_z/J_x)_{\text{est}} \end{bmatrix}, \sigma_J I_2 \right), \quad (10)$$

where  $I_2$  is the  $2 \times 2$  identity matrix.

After sampling each initial state, we run the Broyden-Fletcher-Goldfarb-Shanno (BFGS) algorithm [4, 18, 23, 51] to optimize each sample to a nearby local minimum  $\mathbf{x}_{k,i}(0)$  in the objective function such that:

$$\mathbf{x}_{k,i}(0) = \arg \min_{\mathbf{x}} f(\mathbf{x}), \quad (11)$$

producing a converged initial state  $\mathbf{x}_{k,i}(0)$  which is a good local guess to have produced the observations. In this way, we globally search the solution space up to the density implied by  $n$ . Using a simpler algorithm like gradient descent can still reach convergence, but will take significantly more objective function evaluations due to the high nonlinearity of the attitude inversion problem.

In order to implement this optimization effectively without constraints, it is often necessary to take the absolute value of the intermediate inertia tensor values to maintain physical validity.

## 2.4. Classifying Candidate Solutions

Although all initial conditions will converge to some nearby local minimum, many of these minima will possess a low likelihood determined by  $-\exp(f(\mathbf{x}))$  where  $f(\mathbf{x})$  is the objective function in Equation 4. As we do not generally know how large the geometric and material mismatch between the observed object and the assumed model is, we cannot put a strict bound on a likelihood level that constitutes a high-quality candidate solution. In this work, we identify candidate solutions by choosing a likelihood ratio tolerance  $0 < \ell < 1$ , such that all solutions  $\mathbf{x}_{i,k}(0)$  are candidates for the truth if:

$$e^{-f(\mathbf{x}_{i,k}(0))} > \ell e^{-f(\mathbf{x}_k^*(0))}. \quad (12)$$

Here,  $\mathbf{x}_k^*(0) = \arg \min_{\mathbf{x}_{i,k}(0)} f(\mathbf{x}_{i,k}(0))$  is the highest likelihood solution found after optimization.

## 3. COMPUTING THE LIGHT CURVE

The inversion method in this paper is not dependent on a particular approach for computing light curves and their expected standard deviations. Here, we present the models used to produce the results in Sections 4 and 5.

### 3.1. Object Geometry Definition

We choose to represent the surface geometry of space objects as a polyhedral mesh composed of a collection of flat facets. Each  $i$ th face has  $n_v \geq 3$  or more vertices  $\{v_{i,1}, v_{i,2}, v_{i,n_v}\}$  and an outward-pointing normal vector  $\hat{\mathbf{n}}_i$ . The total facet area is computed for an arbitrary planar polygon via:

$$A(P) = \sum_{j=0}^{k-3} \frac{\|(\mathbf{v}_{j+1} - \mathbf{v}_j) \times (\mathbf{v}_{j+2} - \mathbf{v}_j)\|_2}{2}. \quad (13)$$

In any particular illumination and observation condition, a fraction of the facet's area  $\tilde{a}_i$  might be Sun or observer-shadowed due to obstructing geometry before or after light reaches the surface element, respectively. The remainder of the facet's area  $\bar{a}_i$  is unshadowed and contributes to the total flux reaching the observer from the object, such that the total area of each facet is  $a_i = \tilde{a}_i + \bar{a}_i$ . The geometry for an individual facet is displayed in Figure 1.

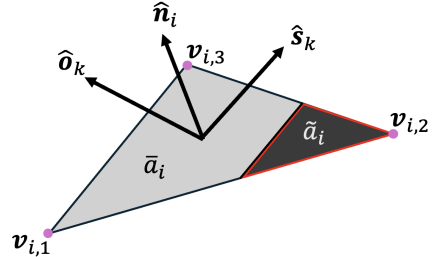


Figure 1: Facet geometry including the observer direction  $\hat{\mathbf{o}}$ , Sun direction  $\hat{\mathbf{s}}$ , normal vector  $\hat{\mathbf{n}}_i$ , unshadowed area  $\bar{a}_i$ , shadowed area  $\tilde{a}_i$ , and counter-clockwise vertex positions  $\{v_{i,1}, v_{i,2}, v_{i,3}\}$ .

In this work, the Sun position is computed using a SPICE ephemeris kernel [31] while space object positions are propagated with SGP4 TLEs obtained from Space-Track [54].

### 3.2. Computing the Unshadowed Area

The unshadowed area  $\bar{a}$  can be computed in several ways. For convex objects,  $\bar{a} = a$  as self-shadowing is impossible. For highly nonconvex and detailed models composed of thousands of faces,  $\bar{a}$  can be approximated on a pixel grid using shadow mapping [44]. Self-shadowing can be efficiently solved semi-analytically for lower-fidelity approximations of real space object geometry by computing the mutual intersections of the polygons  $P_k$  of other faces whose projections overlap with the face in question. Up to a maximum intersection depth  $d$ , selected for computation time, the unshadowed area can be computed via:

$$\bar{a} = a - \sum_{d=1}^n \sum_{K \in \text{comb}(n,d)} (-1)^{d+1} A \left( \bigcap_{k \in K} P_k \right). \quad (14)$$

As the objects we investigate in this work are well-approximated with relatively simple non-convex meshes, we use the semi-analytic method to efficiently compute unshadowed areas via the Sutherland-Hodgeman algorithm [55] for each polygon intersection. Further explanation of the polygon

clipping procedure for computing the total shadowed area, and accelerating this computation during inversion with the so-called shadow cache is available here [46].

### 3.3. Surface Reflectivity

The bidirectional reflectance distribution function (BRDF) defines the amount of incident radiation from  $\hat{\mathbf{s}}$  reflected per steradian in the observer's direction  $\hat{\mathbf{o}}$ . We choose the Blinn-Phong [2] BRDF for this work as it is efficient to compute and satisfies the three main requirements for a physically meaningful BRDF as it is nonnegative, energy-conserving, and reciprocal [12]. We avoid microfacet models for computational efficiency, and because in practice, the uncertainty in the reflective properties of the observed objects will often be larger than errors introduced by the choice of reflection model. The Blinn-Phong BRDF is parameterized by the coefficient of diffuse reflectivity  $C_d$ , the coefficient of specular reflectivity  $C_s$ , and the specular exponent  $n > 0$  [12]:

$$f_r(\hat{\mathbf{s}}, \hat{\mathbf{o}}) = \frac{C_d}{\pi} + \frac{n+2}{2\pi} \frac{C_s(\hat{\mathbf{n}} \cdot \hat{\mathbf{h}})^n}{4(\hat{\mathbf{n}} \cdot \hat{\mathbf{s}})(\hat{\mathbf{n}} \cdot \hat{\mathbf{o}})}. \quad (15)$$

The coefficients of reflectivity implicitly satisfy  $C_a + C_s + C_d = 1$  for energy conservation, where  $0 \leq C_a \leq 1$  is the coefficient of absorption [16].

Here, the halfway vector  $\hat{\mathbf{h}}$  bisects the illumination and observation directions such that  $\hat{\mathbf{h}} = \hat{\mathbf{h}} = (\hat{\mathbf{s}} + \hat{\mathbf{o}}) / \|\hat{\mathbf{s}} + \hat{\mathbf{o}}\|$  [12].

### 3.4. Computing the Mean Observed Signal

Given the observer  $\hat{\mathbf{o}}_k$  and illumination directions  $\hat{\mathbf{s}}_k$  at the  $k$ th observation epoch in the body frame  $\mathcal{B}$ , as well as the BRDF  $f_{r,i}$  for each  $i$ th surface of the object, the fraction of incident power reflected in the direction of the observer is [16]:

$$f_p(\hat{\mathbf{s}}_k, \hat{\mathbf{o}}_k) = \sum_{i=1}^n \mathcal{B}[\bar{a}_i(\hat{\mathbf{s}}_k, \hat{\mathbf{o}}_k) f_{r,i}(\hat{\mathbf{s}}_k, \hat{\mathbf{o}}_k) \cdot (\hat{\mathbf{n}}_i \cdot \hat{\mathbf{s}}_k)(\hat{\mathbf{n}}_i \cdot \hat{\mathbf{o}}_k)]. \quad (16)$$

As many of the noise characteristics of the signal are defined in the image sensor's native unit of ADU, we use  $f_p(\hat{\mathbf{s}}_k, \hat{\mathbf{o}}_k)$  to compute the light curve in ADU via:

$$\bar{S}_{\text{SO},k} = f_p(\hat{\mathbf{s}}_k, \hat{\mathbf{o}}_k) \frac{A_o \Delta t_k f_{\odot}(\mathbf{r})}{g R_{\oplus}^2 r_k^2} \cdot \int_0^{\infty} P(\lambda) Q(\lambda) T_k(\lambda) I_{\odot}(\lambda) \left( \frac{\lambda}{hc} \right) d\lambda. \quad (17)$$

Here before the integral,  $A_o$  is the unobstructed aperture area in square meters,  $\Delta t_k$  is the exposure time in seconds,  $f_{\odot}(\mathbf{r})$  is the fraction of solar irradiance reaching the space object at position  $\mathbf{r}$  – accounting for the Earth's shadow,  $g$  is the sensor gain in ADU per photoelectron,  $R_{\oplus}$  is the distance from the Sun to the space object in AU,  $r_k$  is the distance from the observer to the space object in kilometers. Within the integral, we account for the telescope's passband filter  $P(\lambda)$ , the image sensor quantum efficiency  $Q(\lambda)$ , the atmospheric absorption spectrum  $T_k(\lambda)$ , the solar irradiance spectrum  $I_{\odot}(\lambda)$ , and the inverse energy of a photon with wavelength  $\lambda$ ,  $\lambda/hc$ , where  $h$  is Planck's constant in Joule-seconds, and  $c$  is the speed of light in vacuum in meters per second. Taken together, the integral computes the fraction of the energy reflected from the object absorbed into the image sensor, while the outer factor dimensionalizes the result to yield the mean total sensor response in ADU across all pixels due to the object's signal.

### 3.5. Approximating the Measurement Noise

This section summarizes an in-depth study of relevant noise sources in CCD and CMOS sensor light curves which can be found in [45].

The variance of a space object's observed brightness whose mean is determined by Equation 17 is a combination of many independent stochastic processes. These distributions have variances  $\sigma_{\text{sensor}}^2$  due to the sensor's integration and readout effects,  $\sigma_{\text{flat}}^2$  from sensor flat-fielding effects, scintillation noise  $\bar{S}_{\text{SO},k} \sigma_{Y,k}^2$  [37], Poisson signal shot noise  $\lambda_{\text{shot},k}$ , and Poisson background noise  $\lambda_{\text{back},k}$ . The sum of these variances yields the total signal variance in ADU:

$$\sigma_{\bar{S},k}^2 = \lambda_{\text{back},k} + \bar{S}_{\text{SO},k} \sigma_{Y,k}^2 + \lambda_{\text{shot},k} + \sigma_{\text{flat}}^2 + \sigma_{\text{sensor}}^2. \quad (18)$$

The sensor noise is approximated by the independent combination of Poisson dark current  $\lambda_{\text{dark}}$  and zero-mean Gaussian readout noise  $\sigma_{\text{read}}^2$  [29]:

$$\sigma_{\text{sensor}}^2 = n_{\text{pix}} (\Delta t \cdot \lambda_{\text{dark}} + \sigma_{\text{read}}^2). \quad (19)$$

The flat field noise is modeled as a zero-mean Gaussian linearly scaling with the signal in each of the  $n_{\text{pix}}$

pixels of the object signal  $S_i$  and a constant  $f_k$  fit to the sensor from flat frame observations, yielding the signal standard deviation [36]:

$$\sigma_{\text{flat}}^2 = f_k^2 \sum_{i=1}^{n_{\text{pix}}} S_i^2. \quad (20)$$

The background standard deviation is modeled by the sum of six independent Poisson random processes contributing to light entering the telescope optics from environmental sources. These processes and the sources of their respective models are: scattered moonlight  $\lambda_{\text{moon},k}$  [10], integrated starlight  $\lambda_{\text{star},k}$  [29], twilight  $\lambda_{\text{twi},k}$  [38], zodiacal light  $\lambda_{\text{zod},k}$  [43], airglow  $\lambda_{\text{air},k}$  [29], and light pollution  $\lambda_{\text{poll},k}$  [15, 14]. In summation, the total Poisson background variance is:

$$\lambda_{\text{back},k} = n_{\text{pix},k}(\lambda_{\text{moon},k} + \lambda_{\text{star},k} + \lambda_{\text{twi},k} + \lambda_{\text{zod},k} + \lambda_{\text{air},k} + \lambda_{\text{poll},k}). \quad (21)$$

The fractional scintillation noise due to atmospheric turbulence is modeled via Young’s approximation [37]:

$$\sigma_{Y,k}^2 = 10^{-6} D^{-4/3} (\Delta t)_k^{-1} \cos^{-3}(\gamma_k) e^{-\frac{2h_{\text{obs}}}{H}}. \quad (22)$$

Here, the scintillation noise at timestep  $k$  as a function of the aperture diameter  $D$  in meters, the exposure time  $(\Delta t)_k$  in seconds, the zenith angle  $\gamma_k$ , the observing station’s altitude  $h_{\text{obs}}$  in meters, and the turbulence scaleheight  $H \approx 8000$  meters [37].

The signal shot noise is a Poisson process as a function of the mean signal in ADU  $\bar{S}_{\text{SO},k}$  and the image sensor gain  $g$  in ADU per photoelectron:

$$\lambda_{\text{shot},k} = \frac{\bar{S}_{\text{SO},k}}{\sqrt{g}}. \quad (23)$$

After summation in Equation 18, we can approximate the observed light curve as Gaussian distributed via the mean  $\bar{S}_{\text{SO},k}$  from Equation 17 and the variance  $\sigma_{S,k}^2$  in ADU<sup>2</sup>:

$$S_{\text{SO},k} \sim \mathcal{N}(\bar{S}_{\text{SO},k}, \sigma_{S,k}^2). \quad (24)$$

#### 4. ATTITUDE INVERSION RESULTS FOR SYNTHETIC DATA

To demonstrate the effectiveness of our inversion method, we first present results for a simulated light

curve where the ground truth attitude profile is available for comparison.

##### 4.1. Generating the Simulated Light Curve

To make this simulated case realistic, we use the presented measurement noise models and introduce a mismatch between the ground truth object used to generate the measurements and the model used for inversion. The selected object is a high-fidelity model of the Saturn V second stage scaled down by a factor 10/3 to act as a template rocket body object, shown on the right of Figure 3

Table 1 describes the simulated observation scenario used to produce the noisy light curve observations, placing the rocket body in the orbit of an SL-12 upper stage in geosynchronous orbit, observed by the Purdue Optical Ground Station. Relevant geographical and optical properties of this ground station are provided in the Appendix in Table 9. Table 2 lists the material properties used in this test case.

Table 1: Simulated observation characteristics

Variable	Value
Target COSPAR ID	1990-054D
First obs. (UTC)	Mar 8, 2025 02:00:00.000
Light curve duration	5 minutes
Observations	100
Integration time	0.5 seconds

Table 2: Reflection properties of materials used in the synthetic data test case. The white paint parameters are estimated qualitatively.

Material	$C_d$	$C_s$	$n$
Aluminum [17]	0.34	0.40	8.9
White paint	0.9	0.1	1

The ground truth attitude profile and inertia tensor ratios of the simulated object are listed in Table 3.

Table 3: True object attitude profile for all test cases

Variable	Value
Initial $\mathbf{p}(0)$	$-\frac{1}{3} [1 \ 1 \ 1]^T$
True $\boldsymbol{\omega}(0)$ (rad · s <sup>-1</sup> )	$\boldsymbol{\omega}(0) = [0.03 \ 0.06 \ 0.03]^T$
Inertia tensor ratios	$J_y/J_x = 1, J_z/J_x = 0.25$
External torque $\mathbf{M}$	$[0 \ 0 \ 0]^T$

Simulating the mean light curve and its approximate probability distribution via Equation 24 produces the light curve displayed in V-band magnitude in Figure 2.

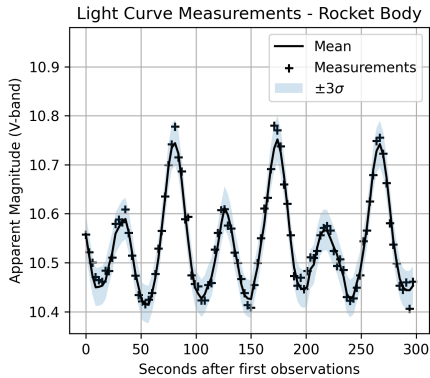


Figure 2: Simulated mean and sampled observations for the rocket body in black in V-band magnitude, with the variance included in blue.

#### 4.2. Case 1U and 1P: Synthetic Light Curve Optimization Results

To emulate the reality that the precise geometry of the observed object is usually uncertain, we use perform attitude inversion with a significantly simplified rocket body model, shown in Figure 3.

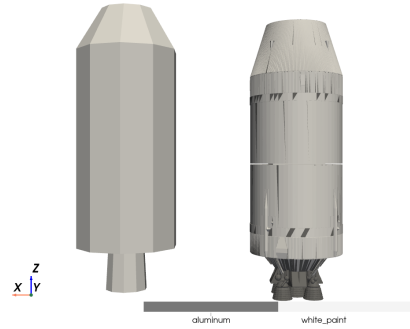


Figure 3: Simplified rocket body model used for inversion (left) and simulated ground truth model (right).

Two distinct inversion cases are computed. Case 1U presents inversion results given no attitude information besides an estimate of the inertia tensor ratios derived from the known geometry – hence requiring a uniform search of the solution space. In contrast, Case 1P presents results given good prior knowledge of attitude state distributions. Table 4 summarizes the initial condition sampling strategies employed for each case. For Case 1P, the standard deviations  $\sigma_\omega$  and  $\sigma_J$  are for spherically-symmetric Gaussians centered on the ground truth. MRPs are sampled by rotating by  $\theta \sim \mathcal{N}(0, \sigma_p)$  degrees away from the ground truth orientation around an axis uniformly sampled on the sphere.

Table 4: Initial condition sampling parameters used for inversion in Cases 1U (no attitude information) and 1P (prior attitude knowledge)

Case 1U	
State	Sampling strategy
$\mathbf{p}$	Uniform, via Equation 9
$\boldsymbol{\omega}$	$\ \boldsymbol{\omega}\ _{\text{mid}} = 5.26$ [deg · s <sup>-1</sup> ], via Eq. 7
$J$	$\sigma_J = 0.1$ , via Equation 10
Case 1P	
State	Sampling strategy
$\mathbf{p}$	Gaussian, $\sigma_p = 20$ [deg]
$\boldsymbol{\omega}$	Gaussian, $\sigma_\omega = 0.1$ [deg · s <sup>-1</sup> ]
$J$	Gaussian, $\sigma_J = 0.05$ [nondim]

For both cases, a total of  $n_{\text{sample}} = 10^5$  initial state samples are created via the sampling schemes described in their respective tables. BFGS minimization is then performed for each initial state sample to locally solve the optimization problem given by

Equation 11. Both cases ran to convergence on an Apple M1 CPU in 3.2 hours.

Solutions are then classified as candidates for the ground truth with  $\ell = 1/2$  via Equation 12. 2026 and 39683 candidate solutions were identified for Cases 1U and 1P, respectively. Figure 4 shows the mean light curves produced by the identified candidate solutions. There is good agreement between the candidate light curves and the observations, indicating that high-quality local minima have been identified.

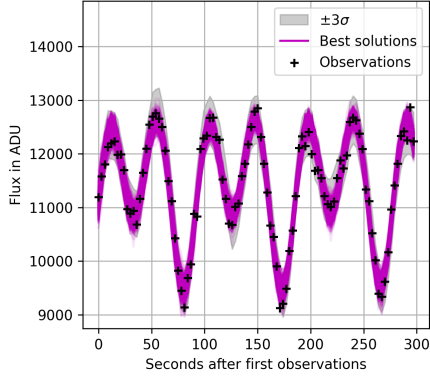


Figure 4: Candidate solution light curves found through BFGS optimization.

Figures 5 and 6 display the candidate MRP and angular velocity of the candidate solutions determined via the procedure detailed in Section 2.4. In the Case 1U figures on the left for orientation and angular velocity, we notice that the ground truth in red lies squarely on a surface containing numerous candidate solutions. This indicates that the local minima have correctly converged to the non-singular subspace of states that approximate the observations well for the assumed shape model. In angular velocity space, shown in Figure 6, most solutions fall onto the surface of two open-ended cylinders – one with half the radius of the larger cylinder containing the truth. Similarly in orientation space, shown in Figure 5, the solutions fall on two distinct manifolds, one containing the truth – likely resulting from a reflection of the object’s body frame about the bisector between the Sun and observer vectors [34, 6]. These additional families of solutions highlight the reality that a wide variety of attitude profiles can produce nearly identical observations.

The Case 1P results on the right within Figures 5 and 6 show that the majority of the initial states sampled close to the truth have converged to a local subset of the solution manifolds identified by Case 1U. We should not expect these solutions to have shrunk down exponentially towards the ground truth – the mismatch in the assumed shape model and the measurement noise inherently limits the minimum size of the feasible solution space.

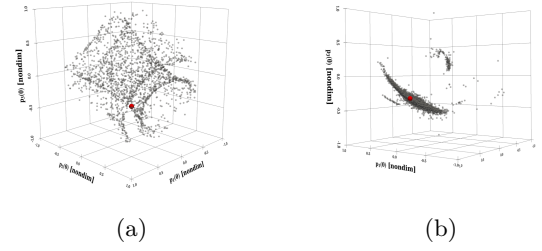


Figure 5: Candidate solution initial orientation MRP vectors for Cases 1U (left) and 1P (right), with the ground truth highlighted in red.

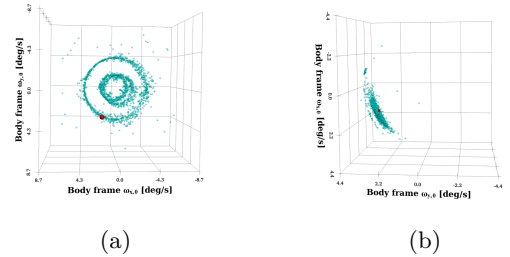


Figure 6: Candidate solution initial body-frame angular velocity vectors for Cases 1U (left) and 1P (right), with the ground truth highlighted in red. Note that each plot shows a unique perspective to highlight the structured distribution of solutions.

Figure 7 displays the inertia tensor solutions for Cases 1U and 1P. Notably, the majority of candidate solutions remain within a few standard deviations of the mean of their initial distribution, with the remaining minority exploring directions that maintain the same precession rate. When a good prior for the other attitude state components is available in Case 1P, the inertia tensor solutions are more well-clustered, although due to the low observability of the rocket body’s spin rate in the observed light curve, there are still ambiguous solutions with higher or lower  $J_z/J_x$  values.

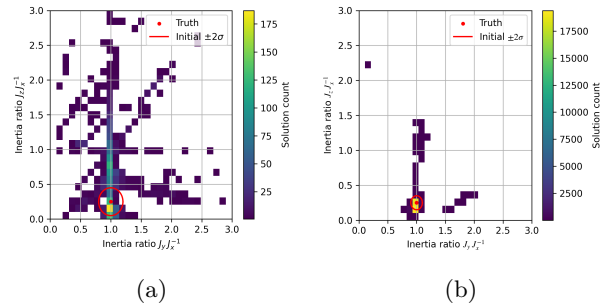


Figure 7: Candidate solution inertia ratios for Cases 1U (left) and 1P (right), with the ground truth highlighted in red.

Figure 8 summarizes the distribution of candidate solutions with respect to the ground truth by displaying the angular velocity magnitude error and angular orientation error compared to the ground truth. Case 1U shows significant variability in angular velocity magnitude, although this is almost entirely due to the unobservability of the spin rate about the object’s axis of symmetry in the light curve. The mean precession rate error is low at 0.3%.

Due to the underdetermined orientation solution space, there are far more solutions at high angular offsets from the truth orientation, leading to a large mean angular error of  $126^\circ$ . For Case 1P, the mean orientation error is much lower at  $18^\circ$ , although convergence here is still inherently limited by the noisy measurements and model mismatch.

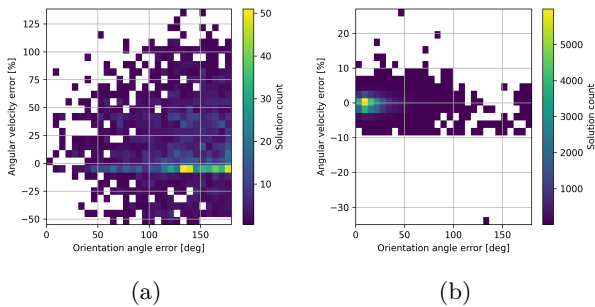


Figure 8: Candidate solution angular orientation error and angular velocity magnitudes for Cases 1U (left) and 1P (right) compared to the ground truth

While introducing a good prior in Case 1P does constrain the solution space, the ambiguities of the light curve inversion problem are still present and lead to the remaining variability we see in Figure 8b. Our method respects this fact and resolves the structure of these surfaces, while other approaches that consider only one solution fail.

## 5. ATTITUDE INVERSION RESULTS FOR REAL DATA

In this section, we provide inversion results for a Delta I upper stage in Case 2D, and the ECHOSTAR II satellite in Case 2E, both observed by the Purdue Optical Ground Station.

### 5.1. Case 2D: Delta I Upper Stage

In Case 2D, we perform attitude inversion on real data observed for a Delta I upper stage rocket body. The chosen Delta I upper stage (COSPAS ID 1984-115C) is a Star-37E [60] solid fuel apogee kick motor,

displayed in Figure 9a. It is  $d = 0.93$  meters in diameter and is approximately  $h = 1.7$  meters in length [61, 30].

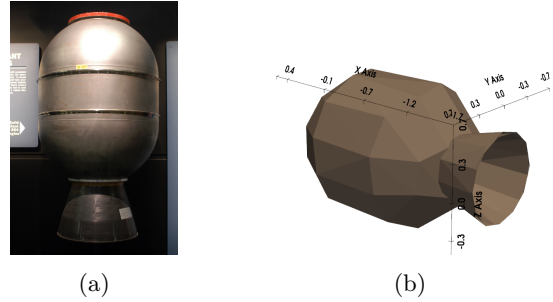


Figure 9: a) Star-37E upper stage [35], b) Simplified model used for inversion.

We compute the inertia tensor of the Star-37E by approximating its geometry as a hollow cylinder of the same aspect ratio such that [50]:

$$J_a = \frac{1}{2}m (r_o^2 + r_i^2) \quad (25)$$

$$J_t = \frac{1}{12}m (3 (r_o^2 + r_i^2) + h^2) \quad (26)$$

$$J_{R/B} = \text{diag} (J_a, J_t, J_t). \quad (27)$$

Here, we choose the inner radius to be  $r_i = 0.45d$ , the outer radius to be  $r_o = 0.5d$ , and  $m = 1$  kilogram – dividing each moment of inertia by a constant does not change the dynamics – yielding  $J_a = 15.3 [kg \cdot m^2]$  and  $J_t = 27.9 [kg \cdot m^2]$ . Table 5 summarizes the light curve observations that result in the extracted measurements displayed in Figure 10.

Table 5: Delta I rocket body observation characteristics

Variable	Value
Target COSPAR ID	1984-115C
First obs. (UTC)	Mar 2, 2025 01:53:30.251
Light curve duration	7.5 minutes
Observations	100 (92 extracted)
Obs. frequency	0.222 Hz
Integration time	3 seconds

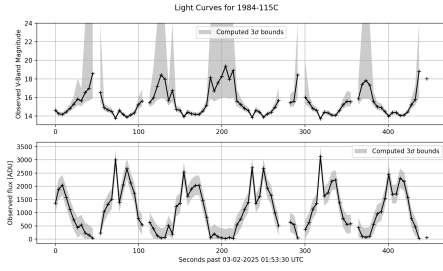


Figure 10: Selected light curve for the Delta I (Star-37E) rocket body, observed by the Purdue Optical Ground Station

This light curve shows clear periodicity but has a high measurement standard deviation and a relatively low sampling rate due to the object’s low brightness and the sensor readout time. Inversion is performed using  $n_{\text{sample}} = 10^4$  samples in 2.4 hours on an Apple M1 CPU. The material and angular velocity assumptions are listed in Table 6. As in Case 1U, orientation, and angular velocity states are sampled via Equations 9 and 7, respectively. All initial inertia tensor samples are set to the estimated  $J_{R/B}$ . The 82 converged candidate solution results are presented in terms of their mean light curves in Figure 11, orientation MRPs and angular velocities in Figure 12, and inertia ratios in Figure 13.

Table 6: Delta I rocket body inversion assumptions

Variable	Value
Uniform BRDF	$C_d = 0.2, C_s = 0.8, n = 30$
$\ \boldsymbol{\omega}\ _{\text{mid}}$	$6.93 \text{ [deg} \cdot \text{s}^{-1}\text{]}$
$\ell$	$1/100$

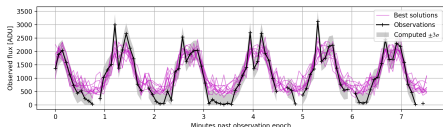


Figure 11: Candidate solution light curves compared to the real measurements in ADU for the Delta I (Star-37E) rocket body.

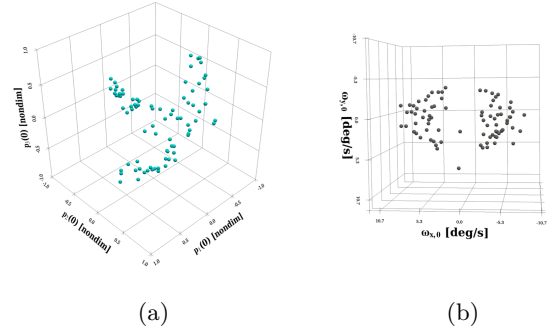


Figure 12: Candidate solution orientation MRPs (left) and angular velocity vectors (right) for the Delta I (Star-37E) rocket body

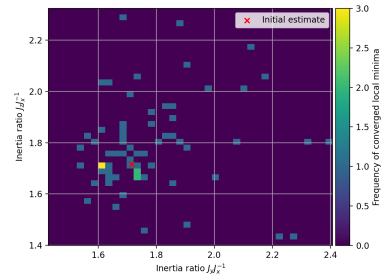


Figure 13: Candidate solution inertia ratio distribution for the Delta I (Star-37E) rocket body

The 82 candidate solutions identified by the inversion process produce light curves that adequately approximate the measurements, although they do not reach the lowest observed values. This indicates that the true material is more dominated by specular reflections than our assumed coefficients. The candidates show some rough clustering in both orientation and angular velocity space, although they vary significantly in angular velocity magnitude. The inertia tensor solutions display similar variability, although the solutions are spread relatively uniformly from the initial estimate, possibly indicating that the geometry-driven estimate is approximately unbiased. Taken together, these results indicate that the object could be spinning in a number of attitude profiles, although the light curve inversion process has significantly narrowed the search space to small subsets of the original unconstrained eight-dimensional volume. These constraints can be combined with additional light curves, information about the object’s true mass distribution, or reflectivity to further refine the solution set.

## 5.2. Case 2E: ECHOSTAR II

In Case 2E, we perform attitude inversion on real data observed for a derelict satellite. ECHOSTAR

II (COSPAR ID 1996-055A) was a communications satellite on the AS-7000 bus [59], shown in Figure 14a. It has an approximate total wingspan of  $s = 23.9$  meters, individual solar panel length of  $l_p = 8.5$  meters, panel width of  $w_p = 3.1$  meters, and a mass per panel of  $m_p = 60$  kilograms [13]. The spacecraft bus is approximately cubic with a side length  $w_b = 2.3$  meters and a mass of  $m_b = 1900$  kilograms [13].

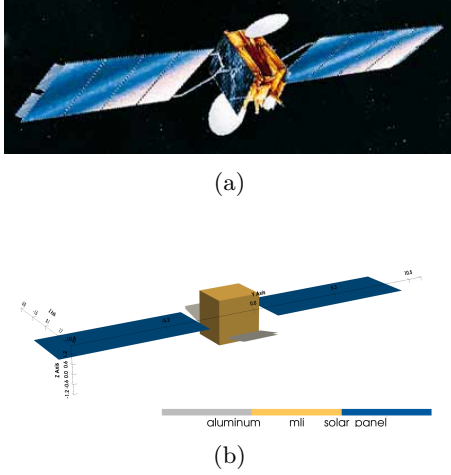


Figure 14: a) Artist's rendition of ECHOSTAR II [59], b) Simplified ECHOSTAR II box-wing model used for inversion.

The contribution of the bus to the total inertia tensor of ECHOSTAR II is spherically symmetric and given by [47]:

$$J_{\text{bus}} = \frac{1}{6} m_b w_b^2 I_3, \quad (28)$$

assuming that the center of mass (COM) of the bus coincides with the COM of the entire vehicle. By the intermediate axis theorem, the contribution of a panel to the inertia tensor is a function of the displacement of the panel's COM from the vehicle's overall COM  $\mathbf{r}_p = [0, s/2 - l_p/2, 0]^T$ :

$$J_{\text{pan}} = \frac{m_p}{12} \cdot \text{diag}(l_p^2, w_p^2, (l_p^2 + w_p^2)) + m_p [(\mathbf{r}_p \cdot \mathbf{r}_p) I_3 - \mathbf{r}_p \mathbf{r}_p^T], \quad (29)$$

assuming that the panels have negligible thickness. The overall inertia tensor for ECHOSTAR II is therefore:

$$J_{\text{SAT}} = J_{\text{bus}} + 2J_{\text{pan}} \quad (30)$$

$$= \text{diag}(9512, 1771, 9609) [kg \cdot m^2] \quad (31)$$

Table 5 summarizes the light curve observations that result in the extracted measurements displayed in Figure 10.

Table 7: ECHOSTAR II observation characteristics

Variable	Value
Target COSPAR ID	1996-055A
First obs. (UTC)	Feb 26, 2025 04:16:12.279
Light curve duration	19.5 minutes
Observations	456 (395 extracted)
Obs. frequency	0.388 Hz
Integration time	1 seconds

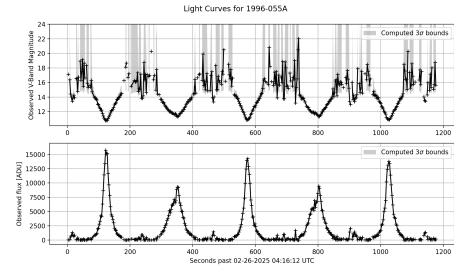


Figure 15: Selected light curve for ECHOSTAR II, observed by the Purdue Optical Ground Station

This light curve is sampled more densely than the Delta I observations and clearly has significantly more intense specular peaks. Inversion is performed using  $n_{\text{sample}} = 10^4$  samples in 48 minutes on an Apple M1 CPU. The material and angular velocity assumptions are listed in Table 8. Initial state sampling is accomplished identically to Case 2D, with a different mean angular velocity and initial inertia ratios. The candidate solution results are presented in terms of their mean light curves in Figure 16, orientation MRPs and angular velocities in Figure 18, and inertia ratios in Figure 17. Since the light curve spans three orders of magnitude with a high signal-to-noise ratio, the shape and material mismatch produces specular peaks that are good fits, but are possibly hundreds of standard deviations away from the computed measurement distribution. To combat this,  $\ell$  is selected to be much more permissive in selecting candidate solutions compared to previous cases.

Table 8: ECHOSTAR II inversion assumptions

Variable	Value
Aluminum BRDF	$C_d = 0.22, C_s = 0.4, n = 5$
MLI BRDF	$C_d = 0.05, C_s = 0.24, n = 20$
Solar panel BRDF	$C_d = 0.05, C_s = 0.13, n = 10$
$\ \omega\ _{\text{mid}}$	$2.32 \text{ [deg} \cdot \text{s}^{-1}]$
$\ell$	$1/1000$

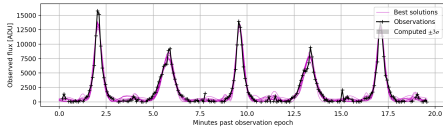


Figure 16: Candidate solution light curves compared to the real measurements in ADU for ECHOSTAR II.

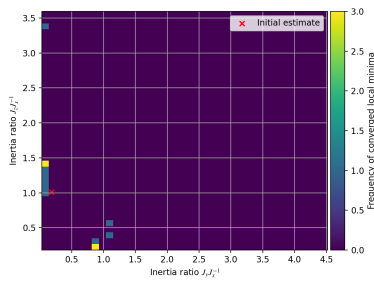


Figure 17: Candidate solution inertia ratio distribution for ECHOSTAR II with the initial estimate in red.

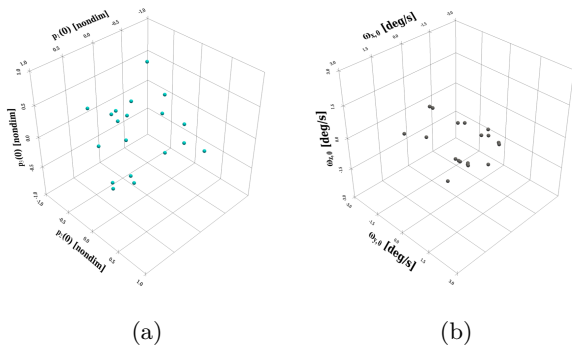


Figure 18: Candidate solution orientation MRPs (left) and angular velocity vectors (right) for ECHOSTAR II

The 19 candidate solutions identified by the inversion process are more sparse than those found in either

of the previous rocket body cases, with some vague clustering in both angular velocity and orientation space. The candidate solution light curves fit the data well. Notably, the formulation of the negative log-likelihood objective function in Equation 4 produces the behavior seen in the candidate solutions in Figure 16, where even the smallest recurrent specular peaks are well-estimated by most solutions. A similar effect – giving up some of the statistical robustness of our formulation – can be achieved in an unweighted optimization over the observations in magnitudes. The inertia tensor solutions are dispersed throughout the solution space, with less symmetry than the Delta I solutions.

As in the Delta I case, the attitude inversion solver has successfully constrained the search space for later optimization as more data about the mass and reflectivity of the object becomes available to continue refining any of these candidates. To address the unknown solar panel rotation angle at the time of ECHOSTAR II’s retirement, a parametric model for the glint timing of the bus and panels could be employed to build an a priori estimate of this angle for more accurate full-state solutions.

## 6. CONCLUSIONS

Attitude information is critical for many tasks informing space situational awareness. Orientation and angular velocity data aid high-fidelity orbit propagation, mission recovery efforts, and object selection for active debris removal. Obtaining attitude information is often difficult, especially for passive debris objects. Due to atmospheric distortion and diffraction-limited optics, ground-based telescopes can only determine the total brightness received from a space object. If a shape model is known, the light curve – a sequence of these brightness measurements – is one tool for attitude estimation in the far field.

We presented an approach for solving this highly nonlinear and non-convex optimization problem with a gradient-based multi-start method. We presented attitude inversion results for one case with synthetic data and two cases with real observations. Results on synthetic data prove that our algorithm converges well to the full set of ambiguous solutions, and that performance improves as more prior information becomes available. Results on real data show that our approach can produce viable clusters of potential full-state solutions even when material properties are unavailable and the assumed geometry is heavily simplified, although convergence becomes less frequent.

Unlike other approaches, our method successfully identifies the numerous ambiguous solution families – originating from symmetries in the observation geometry and the object shape – which can produce the same observations. These disparate candidate solu-

tions can serve as starting points for more detailed exploration as additional light curves or further object shape information is obtained.

## ACKNOWLEDGMENTS

This work was partially supported by a National Defense Science and Engineering Graduate Fellowship.

## APPENDIX

Table 9: Telescope information for synthetic and real data observations

Variable	Value
CCD sensor	KAF-16803
Aperture area ( $A_o$ )	0.076 m <sup>2</sup>
Observer location	32.900° N, −105.533° W
Observer altitude	2.24 km above MSL
Read noise ( $\sigma_{\text{read}}$ )	9 ADU/pixel
Dark current rate ( $\lambda_{\text{dark}}$ )	0.01 ADU/pixel/s
Flat field strength ( $f_k$ )	0.01 (dimensionless)
Gain ( $g$ )	5.1 e <sup>−</sup> /ADU

Table 10: BFGS configuration for all results cases

Variable	Value
Maximum function evaluations	1000
Maximum iterations	100
Finite difference step size	1 · 10 <sup>−5</sup>
Gradient $\infty$ -norm tolerance	1 · 10 <sup>−5</sup>

## REFERENCES

1. Laurence David James Blacketer. Attitude Characterisation of Space Objects using Optical Light Curves. PhD thesis, University of Southampton, March 2022.
2. James F. Blinn. Models of light reflection for computer synthesized pictures. In Proceedings of the 4th Annual Conference on Computer Graphics and Interactive Techniques, SIGGRAPH '77, pages 192–198, New York, NY, USA, 1977. Association for Computing Machinery.
3. Christophe Bonnal, Jean-Marc Ruault, and Marie-Christine Desjean. Active debris removal: Recent progress and current trends. *Acta Astronautica*, 85:51–60, 2013.
4. C. G. Broyden. The Convergence of a Class of Double-rank Minimization Algorithms 1. General Considerations. *IMA Journal of Applied Mathematics*, 6(1):76–90, 03 1970.
5. A Burton and C Frueh. Two methods for light curve inversion for space object attitude determination. In 8th European Conference on Space Debris, 2021.
6. Alexander Burton, Liam Robinson, and Carolin Frueh. Light curve attitude estimation using particle swarm optimizers. *Advances in Space Research*, 2024.
7. Alexander B. Burton, Carolin Frueh, and Liam Robinson. Attitude estimation using light curves: A particle swarm approach. In AIAA SCITECH 2024 Forum, 2024.
8. Ryan Clark, Sidharth Dave, Jack Wawrow, and Regina Lee. Performance of Parameterization Algorithms for Resident Space Object (RSO) Attitude Estimates. In Proceedings of the 20th Advanced Maui Optical and Space Surveillance Technologies Conference, page 14, September 2019.
9. Ryan Clark, Yanchun Fu, Siddharth Dave, and Regina S K Lee. Resident space object (rso) attitude and optical property estimation from space-based light curves. *Advances in Space Research*, 70(11):3271–3280, 2022.
10. G. M. Daniels. A night sky model for satellite search systems. *Optical Engineering*, 16:66–71, February 1977.
11. Andrew D. Dianetti. Resident Space Object Characterization Using Polarized and Multispectral Light Curves. PhD thesis, University at Buffalo, The State University of New York, 2020.
12. Bernardt Duvenhage, Kadi Bouatouch, and Derrick Kourie. Numerical verification of bidirectional reflectance distribution functions for physical plausibility. In SAICSIT '13: Proceedings of the South African Institute for Computer Scientists and Information Technologists Conference, pages 200–208, 10 2013.
13. Michael A. Earl and Gregg A. Wade. Observations of the spin-period variations of inactive box-wing geosynchronous satellites. *Journal of Spacecraft and Rockets*, 52(3):968–977, 2015.
14. Fabio Falchi, Pierantonio Cinzano, Dan Duriscoe, Christopher C. M. Kyba, Christopher D. Elvidge, Kimberly Baugh, Boris Portnov, Nataliya A. Rybnikova, and Riccardo Furgoni. Supplement to: The new world atlas of artificial night sky brightness. v. 1.1. gfz data services. <https://doi.org/10.5880/GFZ.1.4.2016.001>, 2016. Accessed: 2023-08-25.

15. Fabio Falchi, Pierantonio Cinzano, Dan Duriscoe, Christopher C. M. Kyba, Christopher D. Elvidge, Kimberly Baugh, Boris A. Portnov, Nataliya A. Rybnikova, and Riccardo Furgoni. The new world atlas of artificial night sky brightness. *Science Advances*, 2(6):e1600377, 2016.
16. Siwei Fan. The Light Curve Simulation and Its Inversion Problem for Human-Made Space Objects. PhD thesis, Purdue University, August 2020.
17. Forrest Fankhauser, J. Anthony Tyson, and Jacob Askari. Satellite optical brightness. *The Astronomical Journal*, 166(2):59, jul 2023.
18. R. Fletcher. A new approach to variable metric algorithms. *The Computer Journal*, 13(3):317–322, 01 1970.
19. Carolin Früh and Moriba K. Jah. Coupled orbit attitude motion of high area-to-mass ratio (hamr) objects including efficient self-shadowing. *Acta Astronautica*, 95:227–241, 2014.
20. S. Gagnon and John L. Crassidis. Particle swarm optimization on the space of quaternions with applications to attitude estimation from light curves. *Journal of the Astronautical Sciences*, 72(8), March 2025. Accepted 18 February 2025, Published 17 March 2025.
21. Stephen R. Gagnon. Overcoming Convergence Issues With Attitude Determination From Light Curves. PhD thesis, University at Buffalo, The State University of New York, 2024. Copyright - Database copyright ProQuest LLC; ProQuest does not claim copyright in the individual underlying works; Last updated - 2024-02-15.
22. Matteo Gallucci. Light curve inversion for attitude reconstruction of tumbling space debris. PhD thesis, Politecnico di Milano, 2020.
23. Donald Goldfarb. A family of variable-metric methods derived by variational means. *Mathematics of Computation*, 24:23–26, 1970.
24. Joanna C. Hinks and John L. Crassidis. Angular velocity bounds via light curve glint duration. In *Proceedings of the AIAA Guidance, Navigation, and Control Conference*, 2016.
25. Marcus Holzinger, Kyle Alfriend, Charles Wetterer, K. Luu, Chris Sabol, and Kris Hamada. Photometric attitude estimation for agile space objects with shape uncertainty. *Journal of Guidance Control and Dynamics*, 37, 04 2014.
26. G. Isoletta, R. Opromolla, and G. Fasano. Attitude motion classification of resident space objects using light curve spectral analysis. *Advances in Space Research*, 2024.
27. S. Karpov, E. Katkova, G. Beskin, A. Biryukov, S. Bondar, E. Davydov, E. Ivanov, A. Perkov, and V. Sasyuk. Massive photometry of low-altitude artificial satellites on Mini-Mega-TORTORA. In *Revista Mexicana de Astronomia y Astrofisica Conference Series*, volume 48 of *Revista Mexicana de Astronomia y Astrofisica Conference Series*, pages 112–113, December 2016.
28. N Koshkin, L Shakun, E Korobeynikova, S Melikyants, S Strakhova, V Dragomiretsky, A Ryabov, T Golubovskaya, and S Terpan. Monitoring of space debris rotation based on photometry. *Odessa Astronomical Publications*, 31:179–185, 2018.
29. Holger Krag. A Method for the Validation of Space Debris Models and for the Analysis and Planning of Radar and Optical Surveys. PhD thesis, Technische Universität Braunschweig, March 2003.
30. Gunter D. Krebs. Star-37. [https://space.skyrocket.de/doc\\_eng/star-37.htm](https://space.skyrocket.de/doc_eng/star-37.htm). Accessed: 2025-02-26.
31. NASA Jet Propulsion Laboratory. Spice. <https://naif.jpl.nasa.gov/naif/toolkit.html>, 2023. Accessed: 2023-10-24.
32. Richard Linares, John Crassidis, and Moriba Jah. Particle filtering light curve based attitude estimation for non-resolved space objects. *Advances in the Astronautical Sciences*, 152:119–130, 01 2014.
33. Richard Linares, Moriba K Jah, John L Crassidis, and Christopher K Nebelecky. Space object shape characterization and tracking using light curve and angles data. *Journal of Guidance, Control, and Dynamics*, 37(1):13–25, 2014.
34. Simão G. Marto, Massimiliano Vasile, Andrew Campbell, Paul Murray, Stephen Marshall, and Vasili Savitski. Hyperspectral lightcurve inversion for attitude determination. In *Proceedings of the AIAA SCITECH Forum*, 2024.
35. National Museum of the United States Air Force. Thiokol te-m-364-4 solid rocket. <https://www.nationalmuseum.af.mil/Visit/Museum-Exhibits/Fact-Sheets/Display/Article/197693/thiokol-te-m-364-4-solid-rocket>. Accessed: 2025-02-26.
36. Michael Newberry. Pixel response effects on ccd camera gain calibration. Technical report, Mirametrix, Inc., 1996.
37. J. Osborn, D. Föhring, V. S. Dhillon, and R. W. Wilson. Atmospheric scintillation in astronomical photometry. *Monthly Notices of the Royal Astronomical Society*, 452(2):1707–1716, 07 2015.
38. F. Patat, O. S. Ugolnikov, and O. V. Posttyakov. UBVRI twilight sky brightness at ESO-Paranal. *Astronomy and Astrophysics*, 455(1):385–393, August 2006.
39. Fabrizio Piergentili, Fabio Santoni, and Patrick Seitzer. Attitude determination of orbiting objects from lightcurve measurements. *IEEE Transactions on Aerospace and Electronic Systems*, 53(1):81–90, 2017.

40. Fabrizio Piergentili, Gaetano Zarcone, Leonardo Parisi, Lorenzo Mariani, Shariar Hadji Hossein, and Fabio Santoni. Leo object's light-curve acquisition system and their inversion for attitude reconstruction. *Aerospace*, 8(1):4, 2020.
41. Jean-Noël Pittet, Muriel Richard, Dimitri Hollosi, Christophe Paccolat, Volker Gass, Jean-Philippe Thiran, Jiri Silha, and Thomas Schildknecht. Space debris attitude determination of faint leo objects using photometry: Swisscube cubesat study case. In *Proceedings of the 7th ESA space debris conference*, 05 2017.
42. Abdul Rachman. *Understanding Attitude Behavior of Inactive GLONASS Satellites using Spin Period Evolution*. PhD thesis, University of Bern, December 2023.
43. F. E. Roach. A Photometric Model of the Zodiacal Light. *Astronomical Journal*, 77:887, December 1972.
44. Liam Robinson and Carolin Frueh. Light curve inversion for reliable shape reconstruction of human-made space objects. In *Proceedings of the 32nd AIAA/AAS Astrodynamics Specialist Conference*, pages 1–19, 09 2022.
45. Liam Robinson and Carolin Frueh. A ccd/cmso telescope digital twin for space situational awareness. *Advances in Space Research*, 2025. Submitted, Jan. 2025.
46. Liam Robinson and Carolin Frueh. Global light curve attitude estimation with noisy measurements and inertia uncertainty. *Journal of the Astronautical Sciences*, 2025. Submitted, Jan. 2025.
47. John Satterly. The moments of inertia of some polyhedra. *The Mathematical Gazette*, 42(339):11–13, 1958.
48. Ewan Schafer. *Stereoscopic Light Curve Analysis of Space Debris Objects*. PhD thesis, German Aerospace Center (DLR), 12 2017.
49. Thomas Schildknecht, Nikolay Koshkin, Elen Korobeinikova, Seda Melikants, Leonid Shakun, Svetlana Strakhova, Esther Linder, Jiri Silha, and Monika Hager. Photometric Monitoring of Non-resolved Space Debris and Databases of Optical Light Curves. In *Advanced Maui Optical and Space Surveillance Technologies Conference*, page 25, January 2015.
50. Raymond A. Serway and John W. Jewett. *Physics for Scientists and Engineers*. Cengage Learning, 2019.
51. David F. Shanno. Conditioning of quasi-newton methods for function minimization. *Mathematics of Computation*, 24:647–656, 1970.
52. Jiri Silha, Esther Linder, Monika Hager, and Thomas Schildknecht. Optical light curve observations to determine attitude states of space debris. In *Proceedings of 30th International Symposium on Space Technology and Science*, pages 1–5, 12 2015.
53. Jiri Silha, Matej Zigo, Tomas Hrobar, and Peter Jevcak. Light curves application to space debris characterization and classification. In *Proceedings of the 8th European Conference on Space Debris*. ESA Space Debris Office, 04 2021.
54. Space-Track.org. [Space-track.org. https://www.space-track.org/](https://www.space-track.org/), 2023. Accessed: 2023-10-10.
55. Ivan E. Sutherland and Gary W. Hodgman. Reentrant polygon clipping. *Commun. ACM*, 17(1):32–42, January 1974.
56. Hannah Umansky, Kyle Clarke, Rebecca Rogers, Austin Hannon, Jack Kelly, Tristan Latchu, Austin Williams, and Brennan Bryant. Capstone: Recovery and operations of a tumbling small satellite in deep space. In *Proceedings of the Small Satellite Conference*, 2023.
57. David Vallverdú Cabrera, Jens Utzmann, and Roger Förstner. The adaptive Gaussian mixtures unscented Kalman filter for attitude determination using light curves. *Advances in Space Research*, 71(6):2609–2628, March 2023.
58. Alessandro Vananti, Yao lu, and Thomas Schildknecht. Attitude estimation of h2a rocket body from light curve measurements. *International Journal of Astrophysics and Space Science*, 11, 10 2023.
59. Mark Wade. As 7000. <http://www.astronautix.com/a/as7000.html>. Accessed: 2025-02-26.
60. Mark Wade. Delta 3914. <http://www.astronautix.com/d/delta3914.html>. Accessed: 2025-02-26.
61. Mark Wade. Star 37e. <http://www.astronautix.com/s/star37e.html>. Accessed: 2025-02-26.
62. Charles J Wetterer and Moriba Jah. Attitude determination from light curves. *Journal of Guidance, Control, and Dynamics*, 32(5):1648–1651, 2009.
63. V Williams. Location of the rotation axis of a tumbling cylindrical earth satellite by using visual observations: Part i: Theory. *Planetary and Space Science*, 27(6):885–890, 1979.
64. T. Yanagisawa and H. Kurosaki. Shape and motion estimate of leo debris using light curves. *Advances in Space Research*, 50(1):136–145, 2012.